Research Article

Vladimir P. Aleshin*, Eugene A. Grishin, Oleg A. Ivlev, Dmitry D. Novgorodtsev, and Victor D. Shargorodsky

The speckle-interferometric images modelling of artificial Earth satellites in problems of near-Earth astronomy

https://doi.org/10.1515/astro-2018-0020
Received Nov 16, 2017; accepted Dec 27, 2017

Abstract: The article represents the results of efficiency estimation for perspective observation facilities of near-Earth astronomy in terms of the AES (artificial Earth's satellite) optical images obtaining and quality. A mathematical method for modeling optical images based on the induced virtual environment is proposed . A speckle interferometric image registration scheme and bispectral processing are reviewed. Upon modelling, the real speckle interferometric images of stars have been used as scattering functions; the AES orbits and geometry have been set in reliance on the real AES orbits and 3D-shapes. Additionally, photon and readout noises have been modelled. A large set of different variants of the AES orbits and 3D-shapes is reviewed. A non-linear distortion problem is analyzed. The modelling has been performed under various atmosphere turbulence conditions (2", 4"). The following characteristics have been estimated: number of frames to accumulate depending on the AES orbit and shape, noise intensity, type and parameters of bispectral processing, energy characteristics.

Keywords: speckle interferometry, artificial Earth's satellite, bispectral processing

1 Introduction

The real progress in high-quality astronomical imaging under turbulent atmosphere conditions is related to the paper of A. Labeyrie (Labeyrie 1970) which defined the first stage of development for speckle interferometry techniques. A breakthrough in extended object imaging was the triple correlation (bispectral) technique (Lohmann *et al.* 1983) which generalized the Labeyrie's methods. In foreign countries, AES were optically tracked by the Lawrence Livermore National Laboratory (LLNL) scientists using speckle interferometers mainly within the scope of the Strategic Defense Initiative (SDI); the collected data were classified until the early 90's. The results were finally published in 1992 (Lawrence *et al.* 1992). The jointed use of a speckle interferometer and an adaptive optics system at the AMOS station is described in (Roggemann *et al.* 1994). In Russia, speckle interferometry techniques were first implemented at the SAO RAS (large azimuth telescope with the aperture of 6 m) under the supervision of Y. Y. Balega and with the direct involvement of A. Labeyrie and G. Weigelt. The results of these astrophysical experiments are presented in (Balega et al., Rastegaev et al.). At the same place, there was conducted a unique experiment aimed at obtaining optical images of geostationary AES at the diffraction limit of resolution and quantum threshold of sensitivity (range to the AES – about 40,000 km) (Aleshin *et al.* 2011). The observations data were processed on the basis of the analysis of an averaged bispectrum $\widetilde{\boldsymbol{B}}(\boldsymbol{u}, \boldsymbol{v})$ (Aleshin *et al.* 2011a):

$$\widetilde{\boldsymbol{B}}(\boldsymbol{u}, \boldsymbol{v}) = \langle \boldsymbol{B}(\boldsymbol{u}, \boldsymbol{v}) \rangle = \langle \boldsymbol{I}(\boldsymbol{u})\boldsymbol{I}(\boldsymbol{v})\boldsymbol{I}(-\boldsymbol{u}-\boldsymbol{v}) \rangle, \qquad (1)$$

where
$\boldsymbol{I}(\boldsymbol{\omega}) = \Im(\boldsymbol{i})$ ($\boldsymbol{i}$ – measured image, $\Im$ – Fourier transform) (hereinafter $\boldsymbol{\omega}, \boldsymbol{u}, \boldsymbol{v}$ – spatial frequencies),
$\boldsymbol{I}(\boldsymbol{u})\boldsymbol{I}(\boldsymbol{v})\boldsymbol{I}(-\boldsymbol{u}-\boldsymbol{v})$ – instant image bispectrum;
angular brackets $\langle\rangle$ mean ensemble averaging.

Figure 1 and Figure 2 illustrate the examples of collected images (on the left-most frame – one of the AES speckle images; on the mid frame – a restored image; on the right-most frame – a zoomed-in AES image restored

Corresponding Author: Vladimir P. Aleshin: Joint-stock Company Research-and-Production Corporation "Precision System and Instruments", Russian Federation; Email: aleshin_vl@mail.ru
Eugene A. Grishin, Oleg A. Ivlev, Dmitry D. Novgorodtsev, Victor D. Shargorodsky: Joint-stock Company Research-and-Production Corporation "Precision System and Instruments", Russian Federation

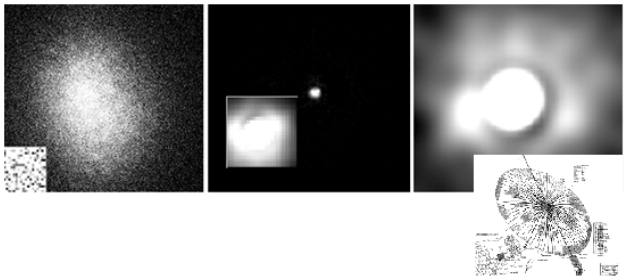

Figure 1. Restored image of the AES «Orion»

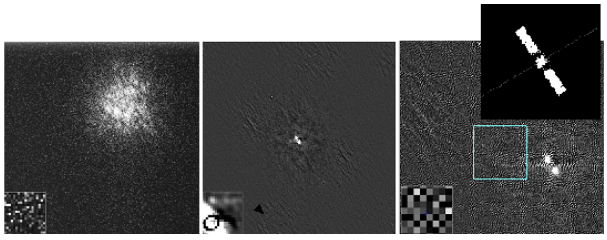

Figure 2. Restored image of the AES «Express AM 2»

through bispectral processing and its 3D-model; the field of view – 4 arcsec).

The difference between images of the low-orbit and geostationary AES is that the images of the LEO AES turn around as the AES move along the orbit, and that needs to be studied separately. In order to analyze the efficiency of speckle interferometry for low-orbit AES imaging with the use of advanced telescopes (Aleshin *et al.* 2016), a full-scale mathematical modelling has been performed.

2 Full-scale mathematical specklegram modelling

The full-scale mathematical modelling technique has been used for modelling purposes. A distortion model has been defined by a linear convolution model (isoplanatic case)

$$\boldsymbol{i} = \boldsymbol{o} \otimes \boldsymbol{h} + \boldsymbol{n}, \tag{2}$$

where
$\boldsymbol{i}$ – measured image,
$\boldsymbol{o}$ – object (AES) image,
$\boldsymbol{h}$ – atmosphere-telescope point-spread function,
$\boldsymbol{n}$ – noises.

Real star images have been used as point-spread functions. For a star (point source) $\boldsymbol{o} = \delta$ and $\boldsymbol{i} = \boldsymbol{h} + \boldsymbol{n}$. The same atmosphere modelling technique was used in (Calef and Therkildsen 2008; Calef Bradoch 2009). AES image modelling $\boldsymbol{o}$ – has been performed using the induced virtual environment technique (Aleshin *et al.* 2004).

2.1 Induced virtual environment

As applied to the present problem, the technique was described in (Aleshin 2016). Now it is illustrated through the chart on Figure 3. The induced virtual environment generates missing parameters of the 3D-scene using external measurements or mathematical modelling.

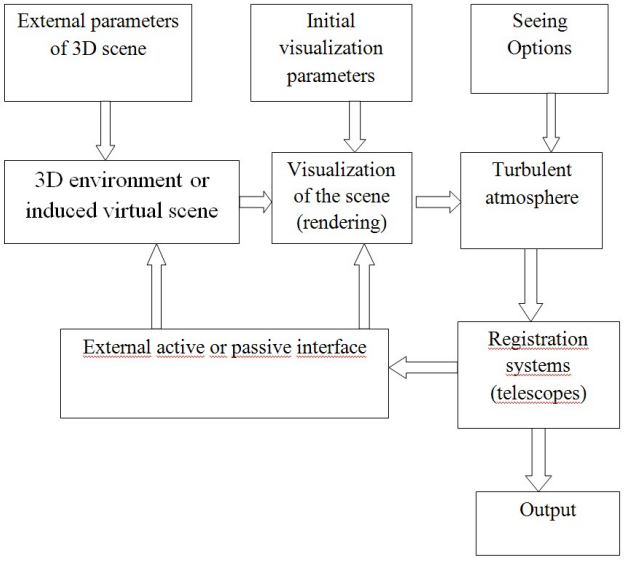

Figure 3. Induced virtual environment technique chart

2.2 Reflectance profile modelling

One of the most common approximations to calculate incoherent reflections from AES is the Kirchhoff approximation (approximation of «tangential plane») (Beckmann and Spizzichino 1963). The Kirchhoff approximation is linear, allowing for quite simple field averaging. Figure 4 illustrates the nature of reflectance (scattering) for various grades of finish: (a) – coherent mirror reflection, (b) – weakly finish surface, (c) – strongly finish surface.

Let us consider the bidirectional reflectance distribution function (BRDF) $\rho_{bd}(\theta_s, \varphi_s, \theta_i, \varphi_i)$ which is defined by the following formula:

$$\rho_{bd}(\theta_s, \varphi_s, \theta_i, \varphi_i) = \frac{\boldsymbol{dI_s}(\theta_s, \varphi_s, \theta_i, \varphi_i)}{\boldsymbol{I_i}(\theta_i, \varphi_i)\cos\theta_i d\omega_i}, \tag{3}$$

where
$\boldsymbol{dI_s}(\theta_s, \varphi_s, \theta_i, \varphi_i)$ – reflectance intensity of the surface el-

ement $d\omega_i$,
$\boldsymbol{I_i}(\theta_i, \varphi_i)$ – incident wave intensity,
$\theta_s, \varphi_s, \theta_i, \varphi_i$ – angles of reflection and incidence in a spherical reference frame.

One of the most general BRDF models is the Beckman-Torrance one (He *et al.* 1991):

$$\rho_{bd} = \rho_{bd,sp} + \rho_{bd,dd} + \rho_{bd,ud}, \tag{4}$$

where
ρ_{bd} – full bidirectional reflection,
$\rho_{bd,sp}$ – mirror component,
$\rho_{bd,dd}$ – diffusion systematic component,
$\rho_{bd,ud}$ – diffusion uniform component (Lambertian).

Ratios for the bidirectional scattering functions in the given approximation are as follows:

$$\rho_{bd,sp} = \frac{\rho_s}{\cos\Theta_i d\omega_i} \cdot \Delta = \frac{|F|^2 \cdot e^{-g} \cdot S}{\cos\theta_i d\omega_i} \cdot \Delta, \tag{5}$$

$$\rho_{bd,dd} = \frac{\Im\left(\hat{n}_b, \hat{n}_b, p\right) \cdot S}{\cos\theta_i d\omega_i} \cdot \frac{\tau^2}{16\pi} \cdot \sum_{m=1}^{\infty} \frac{g^m e^{-g}}{m! \cdot m} \cdot exp\left(-\frac{v_{xy}^2 \tau^2}{4m}\right), \tag{6}$$

$$\rho_{bd,ud} = a(\lambda), \tag{7}$$

$$g = \left[\frac{2\pi\sigma}{\lambda}\left(\cos\theta_i + \cos\theta_s\right)\right]^2, \tag{8}$$

where
g – function for efficient surface roughness (σ – RMS deviation of the surface roughness height fluctuation,
λ – emission wavelength),
τ – surface roughness correlation coefficient,
$|F|^2$ – Fresnel material reflectance,
S – shading function,
$\Im\left(\hat{n}_b, \hat{n}_b, p\right)$ – coefficient considering Fresnel reflection and polarization p,
Δ – function which defines the angle of mirror reflection.

The Torrance-Sparrow (Torrance and Sparrow 1967) and Cook-Torrance (Cook and Torrance 1982) models are particular cases of the above-mentioned model.

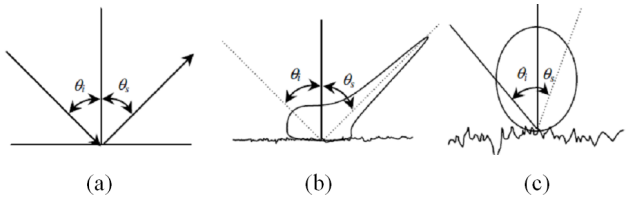

Figure 4. Types of reflectance for various grades of surface roughness

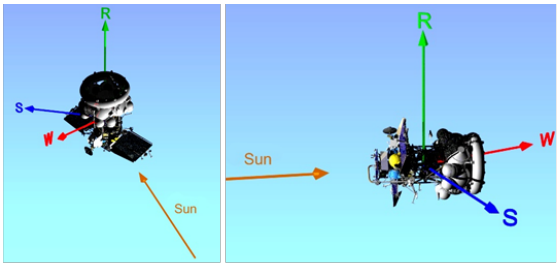

Figure 5. Orientation of the spacecraft «Phobos-Grunt» on 29.11.2011 (on the left) and on 23.12.2011 (on the right)

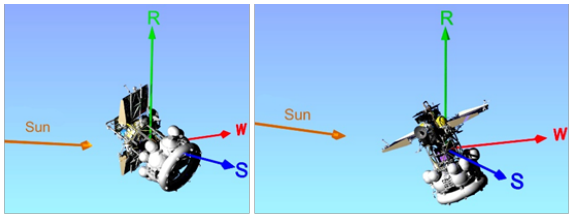

Figure 6. Orientation of the spacecraft «Phobos-Grunt» on 24.12.2011 (on the left) and on 25.12.2011 (on the right)

2.3 AES orientation change modelling upon its motion along the orbit

For AES orientation modelling in its relation to a telescope and the Sun, the real orbit and astropredictions have been used. AES motion relative to the center of mass has been defined in accordance with the classic paper of (Beletsky 1965). The analysis has been performed in an orbital reference frame (**R**, **S**, **W** axes), where **R** – radius vector from the geocenter, **S** – tangent to the orbit in the direction of the velocity vector, **W** – basis vector (binormal) complementing **R**, **S** to the right-hand triple. Figure 5 and Figure 6 show orientation modelling variants for the AES «Phobos-Grunt» using the induced virtual environment technique. To find more details about it, one can check the respective astro-ballistic modelling given in (Novgorodtsev *et al.* 2011; Aleshin *et al.* 2011; Aleshin 2013).

One of the most difficult parts of the low-orbit AES analysis compared to the geostationary ones is a turnaround of the orbital reference frame (RF) in relation to the telescope. Image orientation changes even in case of the AES stabilized in the orbital RF. Figure 7 shows the sequence of the AES images upon its motion along the real orbit. The image reference frame is tied up to the telescope. The last part of images corresponds to AES passing through the culmination point.

Figure 7. Sequence of AES images upon its motion along the real orbit

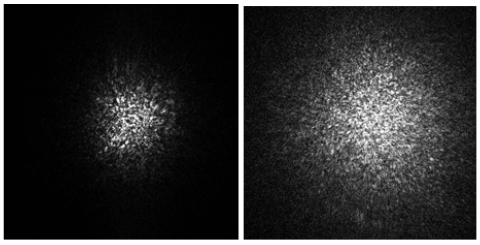

Figure 8. Star specklegrams (on the left – star №1, on the right – star №2)

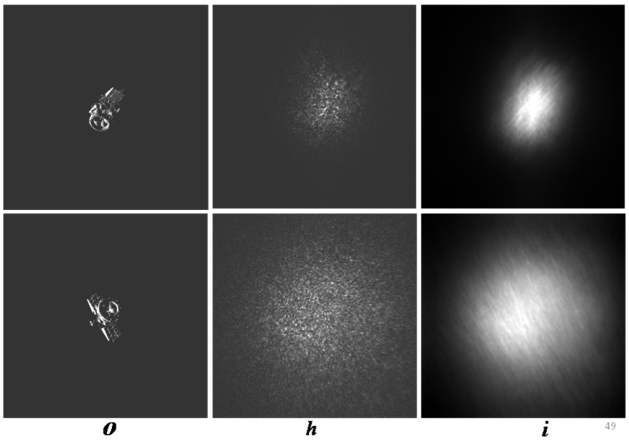

Figure 9. AES image convolution and atmosphere point-spread function

2.4 Turbulent atmosphere and specklegram modelling

As an atmosphere model, we have used real measurements (specklegrams) of stars collected through the 6 m telescope (LAT) of the SAO RAS. The following stars have been considered (numerated by the SAO RAS catalogue): star №1 – FRCet_550_200f, star №2 – 18Leo_550_200fr. Single specklegrams (for shortly expositional star images) are given on Figure 8.

Figure 9 gives measured AES images modelled using the AES true image convolution and a star image. The upper row corresponds to the star №1, the bottom one– to the star № 2.

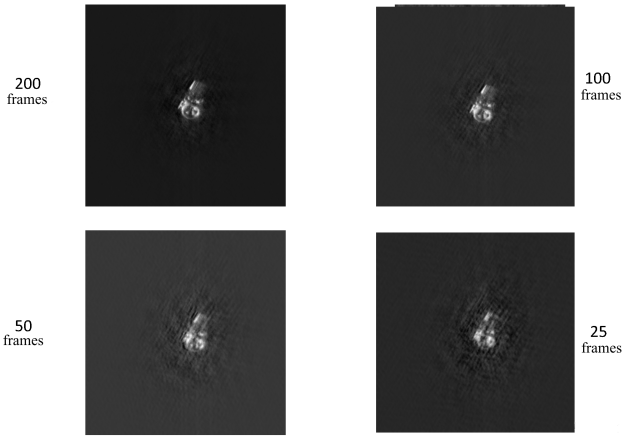

Figure 10. Restored images (point-spread functions– star №1)

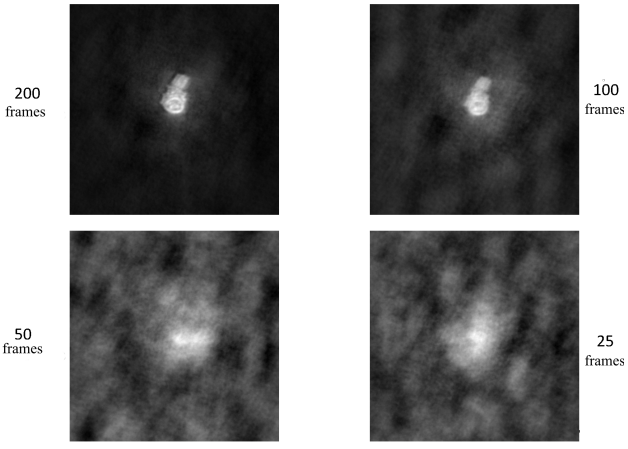

Figure 11. Restored images (point-spread functions – star №2)

3 Image restoration

The images have been restored using bispectral processing (triple correlation technique (Lohmann *et al.* 1983; Aleshin *et al.* 2011b). Figure 10 gives a series of restored images (point-spread functions – star №1). Each frame also gives the number of accumulation frames (specklegrams) used upon restoration.

Figure 11 illustrates a series of restored images for the star №2.

3.1 Noises and non-linear effects

Upon photon noise modelling, a Gaussian non-stationary noise model has been used, which was applied, for example, in Calef Bradoch (2009). Figure 12 represents the restored images.

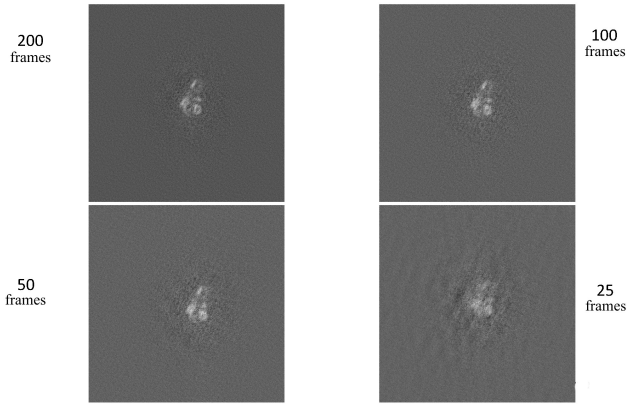

Figure 12. Restored images for photon noises (point-spread functions – star №1)

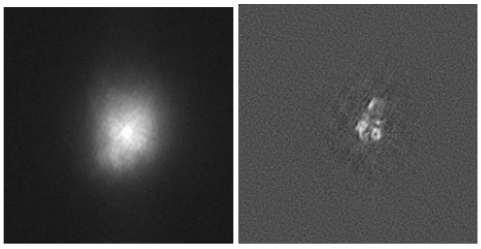

Figure 13. Readout noises (left image). Images restored through 50 frames (right image)

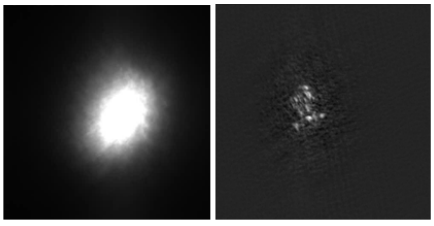

Figure 14. Non-linear effects (left image) and images restored through 70 accumulation frames (right image)

Readout noises (Figure 13) and non-linear distortions (Figure 14) have been reviewed separately.

3.2 Rotation of images of low-orbit AES upon their passing in the vicinity of the culmination point

The most critical case of EAS image restoration is an orbit segment covering the culminaton (zenith) area. As an example, see the last part of images on Figure 7. In that case, one cannot accumulate too many frames. For the modelling we have selected 25 accumulation frames. The obtained restored images are presented on Figure 15.

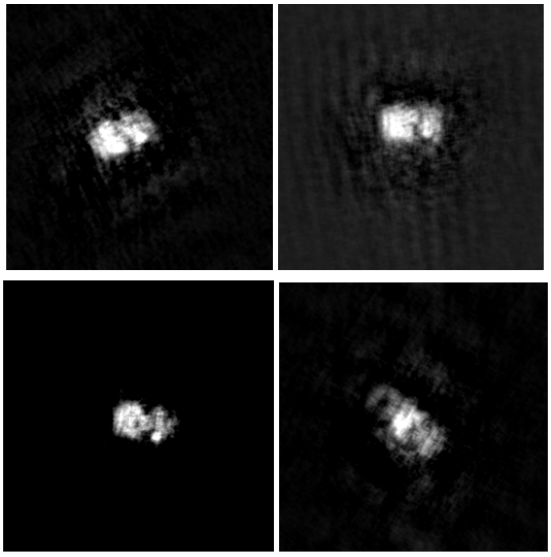

Figure 15. Images subsequently restored through 25 accumulation frames in the culmination area

The obtained restored images are at the bottom limit of adequate interpretation.

4 Conclusions and discussion

1. The modelling has shown the efficiency of bispectral processing for the reviewed category of tasks.
2. Upon selecting the length of a processed frame sequence segment, one needs to be guided by 2 criteria: first, the length must be the largest possible one in order to eliminate redundant speckle noises; second, there must be no «smearing» due to the orbital RF turnaround in relation to the telescope. A theoretical number of averagings (frames) is determined by a number of aperture closure triangles (about a few hundred). Upon that, the signal-noise ratio also increases (proportionally to the square root of the number of frames).
3. Frame number limit is determined by the change of a sought image due to the orbital reference frame turnaround and change of visible SC sizes upon its motion along the orbit. According to the numerous modelling experiments, the minimum number of frames in the culmination area for objects like the faulty «Phobos-Grunt» and such is equal to 20-25 (25 Hz rate). Otherwise, an image is «smeared» due to the turnaround. As demonstrated in the modelling, restored images are at the limit of interpretation possibility (see Figure 15).

4. The most probable processing range is 50-100 frames, providing restored images of decent quality (Figure 10-12).
5. To enhance the restoration efficiency for the purposes of increasing the number of accumulation frames, one can perform a compensating turnaround of images based on the use of the induced virtual environment.

References

Aleshin V. P., Afanasev V.O. Baygozin D.A., Baturin Y.M., Klimenko S.V. 2004, Proc. of 14th Int. Conf. "GraphiCon-2004", MSU, 2004, 12-15(in Russian)

Aleshin VP, Balega Yu.Yu., Maksimov AF, Komarinsky SL, Novgorodtsev D.D. 2011a Vestnik of SibSAU. 6 (39). 154-158 (in Russian)

Aleshin VP, Grishin EA, Ivlev OA, Novgorodtsev D.D., V.D. Shargorodsky V.D. 2016, Kinematics and Physics of Celestial Bodies, 32(5), Allerton Press, Inc., 2016, 256-260.

Aleshin, V.P, Grishin, E.A., Inshin, P.P., Novgorodtsev, D.D., Shargorodsky, V.D., 2011 Electromagnetic Waves and Electronic, 16(3), Moscow, 30-35(in Russian)

Aleshin, V.P. 2013, Ecological bulletin of scientific centers of the Black Sea Economic Cooperation] 3(4) 7-12(in Russian)

Aleshin, V.P. 2016, Proc. of 26 conference 'Graphicon-2016", M., Protvino, ICPT Publ., 2016, 9–13(in Russian)

Aleshin, V.P., Balega, Yu.Yu., Grishin, E.A., Maksimov, A.F., Dyachenko, V.V., Malogolovets, E.V., Komarinsky, S.L., Novgorodtsev, D.D., Shargorodsky, V.D., 2011b Electromagnetic waves and electronic systems. 16(3). 9-17 (in Russian)

Aleshin, V.P., Novgorodtsev, D.D., Vygon, V.G., Grishin, E.A., Shargorodsky V.D. 2011, Vestnik SibSAU, 6 (39) 2011, 159-165 (in Russian)

Balega, Y., Blazit, A., Bonneau, D., Koechlin, L., Foy, R. and Labeyrie, A. 1982, Astron. Astrophys. 115, 253-256.

Beckmann P., Spizzichino A. 1963, The Scattering of Electromagnetic Wave from Rough Surfaces, Pergamon Press, 1963

Beletsky V.V. 1965, Motion of an artificial satellite relative to the center of mass, M., Nauka, 1965,. Beletsky V.V. 1966, Israel program for scientific translations. Jerusalem, translated from Russian, 1966.

Calef Brandoch 2009, Proceedings of the AMOS Technical Conference 2009, 120-126.

Calef, B. and Therkildsen, E. 2008, Proceedings of the AMOS Technical Conference 2008, 287-295.

Cook R.L., Torrance K.E. 1982 ACM Transaction on Graphics, 1(1).

He X.D., Torrance K.E, Sillion F.X, Greenberg D.P. 1991, Computer Graphics, 25(4), 175-18.6

Labeyrie Antoine 1970, Astronomy and Astrophysics, 6, 85-87.

Lawrence T.W., Goodman D.M., Fitch J.P. 1992, Appl. Opt. 31, 1992, 6307-6321.

Lohmann, A.W., Weigelt, G., Wiritzer, B.1. 1983 Applied Optics, 22, 4028-4037.

Novgorodtsev, D.D, Aleshin, V.P, Grishin, E.A, Yurasov, V.S., 2011, Electromagnetic waves and electronic systems, 16(3), 18-29, (in Russian)

Rastegaev, D.A., Balega, Yu.Yu., Maksimov, A.F., Malogolovets, E.V., Dyachenko, V.V. 2008, Astrophysical Bulletin, 63(3), 278-289 (in Russian)

Roggemann, M.C., Caudill, E.L., Tyler, D.W., Fox, M.J., VonBokern, M.A.,and Matson C.L. 1994, Appl. Opt. 33, 3099-3110.

Torrance K.E., Sparrow E.M. 1967 Journal of the Optical Society of America, JOSA, 57(9), 1105-1114.